ACS EARTH AND SPACE CHEMISTRY

http://pubs.acs.org/journal/aesccq

Article

Carbon Monoxide in Optically Thick Wildfire Smoke: Evaluating TROPOMI Using CU Airborne SOF Column Observations

Jake P. Rowe, Kyle J. Zarzana, Natalie Kille, Tobias Borsdorff, Manu Goudar, Christopher F. Lee, Theodore K. Koenig, Johana Romero-Alvarez, Teresa Campos, Christoph Knote, Nicolas Theys, Jochen Landgraf, and Rainer Volkamer*

Cite This: *ACS Earth Space Chem.* 2022, 6, 1799–1812

Read Online

ACCESS | Metrics & More | Article Recommendations | Supporting Information

ABSTRACT: TROPOspheric Monitoring Instrument (TROPOMI) measurements of carbon monoxide (CO) vertical column enhancements in optically thick biomass burning plumes were evaluated using measurements from the University of Colorado Airborne Solar Occultation Flux (CU AirSOF) instrument during the 2018 Biomass Burning Fluxes of Trace Gases and Aerosols (BB-FLUX) field campaign in the northwestern United States. The different temporal and spatial scales and measurement geometries sampled from the aircraft and satellite are actively accounted for by (1) focusing on coincident measurements, (2) comparing spatial integrals of CO enhancements across plume transects, (3) using the FLEXible PARTicle (FLEXPART) dispersion model to correct for atmospheric transport, and (4) accounting for Averaging Kernels (AVK). TROPOMI is found to be systematically higher relative to the aircraft by +36% for the operational product (+27% preoperational product) without geospatial and temporal corrections. Consecutive transects by CU AirSOF revealed significant variations between integrated CO enhancements (on average 28% over 30 min) on the satellite sub-pixel scale. When the additional corrections are applied (FLEXPART, and to a lesser degree also AVK), the average bias is reduced to +10% for the operational product (+7.2% preoperational), which is insignificant within 15% uncertainty (variability among case studies, 95% confidence level). Radiative transfer simulations in synthetic plumes indicate that multiple scattering can enhance satellite CO signals by 5−10% at high aerosol loads, which warrants further attention. Smoke strongly reduces trace gas measurements at ultraviolet and visible wavelengths (by up to a factor of 6), highlighting the importance of multispectral aerosol properties in thick smoke.

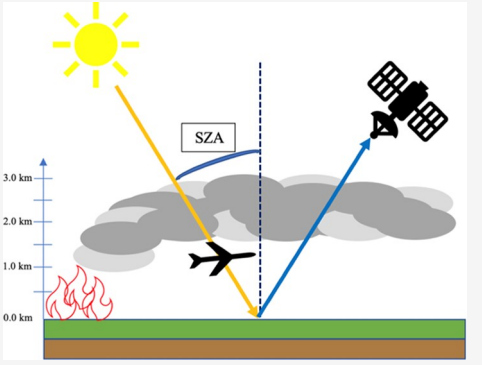

KEYWORDS: *biomass burning, TROPOMI, carbon monoxide, vertical column densities, remote sensing, satellite evaluation*

1. INTRODUCTION

Wildfires are important sources of aerosols and many atmospheric trace gases,[1] and have far-reaching impacts on global ecosystems and human health.[2−5] Studies suggest that wildfire frequency will continue to increase due to global climate change.[6,7] The National Academy of Sciences recognizes the need to better quantify emissions of gases from wildfires as a priority area for future atmospheric chemistry research,[8] with the goal of predicting a net flux using models. Sampling wildfires pose many challenges as fires often ignite sporadically in remote regions that are hard to access from the ground. While research aircraft can efficiently sample wildfire plumes, they are often not available for the entire fire season and are often unable to sample close to the fire. Conversely, satellite instruments like the TROPOspheric Monitoring Instrument (TROPOMI) can measure directly over plumes and can provide daily coverage over the entire globe with a high spatial resolution, but these measurements require validation from ground or airborne platforms (e.g., Borsdorff et al.;[9,10] Theys et al.;[11] Guo et al.;[12] Sha et al.[13]). Of the species emitted by fires, carbon monoxide (CO) is the single most abundant reactive carbon species and is well suited for measurements due to its large emissions from biomass burning[14] and its long atmospheric lifetime.[15,16]

Several aircraft campaigns examining wildfires were conducted in the northwestern United States during the summer of 2018, including the Western Wildfire Experiment for Cloud Chemistry, Aerosol Absorption, and Nitrogen (WE-CAN; e.g., Permar et al.;[17] Juncosa Calahorrano et al.;[18] Lindaas et al.[19]) and the Biomass Burning Fluxes of Trace Gases and Aerosols field campaign (BB-FLUX; Volkamer et al.[20,21]). The BB-FLUX campaign incorporated the use of innovative remote

Received: March 20, 2022
Revised: May 25, 2022
Accepted: May 31, 2022
Published: June 16, 2022

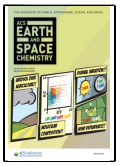

Table 1. BB-FLUX Research Flights and AirSOF Codes, where PUN_C-## Stands for a Plume Underpass, and the Respective Occurrence of That Underpass (See Text S2)[a]

date	flight number	fire name	BB-FLUX underpass and sampling time	Lat/Lon sampling range	TROPOMI orbit number	TROPOMI overpass time	ΔTime (HH:MM)	% CO column above plane
Aug-02	RF05	CA smoke river	PUN_C-01 19:58:50−20:36:37	[40, 42.5] [−119.0, −117.0]	4163	20:30:00	−00:12	99
Aug-08	RF09	Rabbit	PUN_C-01 21:11:45−21:16:45	[44.5, 45.5]	4248	20:20:00	00:54	97
		Foot	PUN_C-02 21:21:32−21:27:38	[−114.5, −113.0]			01:05	98
Aug-12	RF11	Rabbit	PUN_C-07 19:59:47−20:05:14	[44.5, 46.0]	4305	20:45:00	−00:42	100
		Foot	PUN_C-08 20:07:04−20:14:44	[−115.0, −112.5]			−00:34	100
Aug-15	RF13	Rabbit	PUN_C-04 21:08:09−21:17:22	[44.3, 45.8]	4348	21:30:00	−00:17	[b]
		Foot	PUN_C-05 21:23:46−21:33:07	[−115.0, −112.5]			00:02	
Aug-19	RF15	Watson	PUN_C-02 21:50:16−21:55:01	[42.0, 44.5]	4405	21:54:00	−00:01	96
		Creek	PUN_C-03 21:58:22−22:03:12	[−122.0, −119.0]			00:07	94
Aug-25	RF21	Watson	PUN_C-04 19:44:29−19:48:59		4489	20:00:00	−00:13	98
			PUN_C-05 20:04:32−20:10:18	[42.0, 44.5]			00:07	100
		Creek	PUN_C-06 20:13:04−20:20:03	[−122.0, −119.0]			00:17	97
			PUN_C-07 20:20:50−20:27:36				00:24	101
Aug-25	RF22	Watson	PUN_C-01 22:34:29−22:40:25	[42.0, 44.5]	4490	21:41:00	00:55	99
		Creek	PUN_C-02 22:42:40−22:48:52	[−122.0, −119.0]			01:05	92

[a]All times displayed are in UTC, and all flights were conducted in 2018. Delta times compare the TROPOMI orbit time to the center aircraft underpass time. [b]Indicates in situ CO instrument was not working and a % column could not be calculated.

sensing instruments developed to better quantify emission fluxes of trace gases from wildfires.[20,22−24] From the foundation provided in Kille et al.,[22] airborne CO column measurements can be compared with those measured by satellites. This study focuses on TROPOMI[25] onboard the Sentinel-5 Precursor (S-5P) satellite, which provides total vertical column measurements of CO and methane (CH_4[26−28]) with daily global coverage at high spatial resolution retrieved from the shortwave-infrared (SWIR) measurements. The TROPOMI CO dataset has already been used to detect pollution in cities and suburbs, as well as from traffic along main roads.[9,29−31] The TROPOMI CO dataset was validated with TCCON (Total Carbon Column Observing Network[32]) measurements that show the dataset fulfills the mission requirements (10% precision and 15% accuracy for single soundings[9,10,13,33]). However, the measurements of the TCCON stations are mainly remote from pollution sources and represent the CO background concentration. Borsdorff et al.[9] used ground-based Network for the Detection of Atmospheric Composition Change (NDACC) measurements to validate the TROPOMI CO dataset for polluted scenes in Mexico City. In that study, good agreement between satellite and ground-based measurements required strict collocation and temporal criteria due to highly variable CO columns.

Data from the ultraviolet−visible (UV−vis) detector on TROPOMI have been used to derive biomass burning trace gas emissions and lifetimes,[34,35] proxies for combustion efficiency,[36] and to study direct emissions of CO (e.g., Borsdorff et al.[31] and Vellalassery et al.[37]). However, to the best of our knowledge, direct comparisons of TROPOMI CO columns with aircraft column measurements for biomass burning events have not yet been performed and hold the potential to improve the characterization of global wildfire emissions. In complex environments affected by wildfire smoke, airborne column measurements are particularly well suited for satellite validation, as they can position the sensor close to the smoke source to integrate over horizontal and vertical heterogeneities inside the plume. The University of Colorado Airborne Solar Occultation Flux (CU AirSOF) instrument retrieves CO columns in nearly the same spectral range as TROPOMI using measurements along the direct solar beam[22] and thus provides an excellent dataset for comparison with TROPOMI.

This study addresses a fundamental sampling challenge that consists of the different spatial and temporal sampling scales of the aircraft and satellite. CO columns are vertical concentration integrals and are further integrated horizontally across the plumes; the data are then time-aligned with dispersion models[38−41] to correct for the downwind transport of CO. While in situ and column CO measurements have both been successfully used to normalize the relative abundances of trace gases and aerosols in wildfire smoke (e.g., Akagi et al.;[2] Andreae;[15] Kille et al.[22]), satellite measurements of CO in context of other trace gases[11,34−36] require to consider radiative transfer,[11,42] in particular the wavelength dependence of aerosol scattering and absorption of solar photons in the smoke plume. Section 2 describes active measures taken in this study to deal with the fundamental sampling challenge in time

https://doi.org/10.1021/acsearthspacechem.2c00048
ACS Earth Space Chem. 2022, 6, 1799−1812

and space, and introduces case studies and radiative transfer simulation tools used to assess the (multispectral) effects of aerosols in thick wildfire smoke. Section 3 aims to better understand the accuracy of CO column enhancements to better quantify wildfire emissions (e.g., Bela et al.;[43] Burling et al.;[44] Kille et al.;[22] Volkamer et al.[20]) and assess the uncertainties due to aerosols in optically thick smoke plumes. The results from the measurement comparisons are explored in Sections 3.1−3.4, followed by an error budget, bias assessment in thick wildfire smoke, radiative transfer simulations to assess the effects of aerosols in thick wildfire smoke at different wavelengths, and Section 4.

2. METHODS

2.1. BB-FLUX Campaign. The BB-FLUX field campaign (https://volkamergroup.colorado.edu/timeline/field/bb-flux) took place during the 2018 western U.S. wildfire season, with the primary goal of better quantifying emissions from wildfires.[20,21] CU AirSOF was deployed on the University of Wyoming King Air to calculate the emission fluxes of trace gas for these wildfires across 37 research flights (RFs).[20−22] Additional mission objectives included characterizing plume dynamics, such as injection height, and studying the secondary production of ozone in wildfires. Of particular interest for this study was exploring the synergies of suborbital and orbital measurements of biomass burning plumes. The aircraft was positioned to fly underpasses below the plumes, with the goal of capturing the full plume column above the plane from direct-sun absorption measurements with CU AirSOF at infrared wavelengths.[22] Trace gases, including CO and NH_3, were targets from underpasses of biomass burning plumes. Profile shape information was determined using in situ measurements during vertical profiles through the plume. Similar profiles were also taken outside the plume to characterize the background.

In total, 143 successful underpass measurements were performed during BB-FLUX, and the ones listed in Table 1 were selected for comparison to TROPOMI, with Figure 1 illustrating the orbital perspective of a subset of these cases sampled from the Rabbit Foot and Watson Creek fires during August 2018. More details on the mission objectives and design of the BB-FLUX project can be found in Volkamer et al.[20]

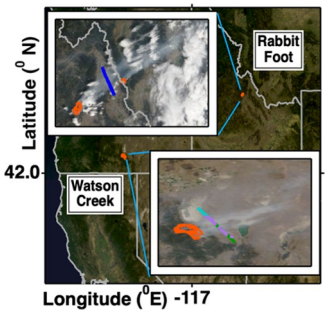

Figure 1. Overview map of the fires of interest sampled during the 2018 BB-FLUX campaign. Of the 37 total research flights (RFs), 5 are chosen for comparison in this study. Insets for each wildfire probed showcase a visible stationary image for a single day's measurements. The Rabbit Foot image was taken on 12 August 2018, and the Watson Creek image on 25 August 2018, via NASA Worldview. Overlaid are the extracted flight tracks where aircraft measurements were taken, as well as fire perimeters (orange traces) for a given day.

2.2. CU Airborne Solar Occultation Flux. The CU AirSOF instrument is described in Kille et al.[22] for applications to biomass burning plumes during BB-FLUX. The instrument operates under the principles of Fourier transform spectroscopy (FTS) and incorporates motion-stabilized optics for real-time solar tracking through a zinc selenide viewport in the top of the plane. To measure CO in the SWIR regime, vibrational overtone bands from 2350 to 2373 nm (4214−4254 cm^{-1}) are fit from spectra captured by CU AirSOF using SFIT4 v0.9.4.4[45] with fit settings described in Table S1. The CO cross section used for the fit is from the HIgh Resolution TRANsmission 2012 (HITRAN[46]) database.

By design, CU AirSOF measures a vertical column density (VCD) due to the motion-stabilized solar tracking maintaining a direct-sun geometry. The solar zenith angle provides the necessary correction to convert the slant column to a vertical column. Here, the threshold of success to accept an SFIT4 CO column, when using the CO VCD measurements, includes three criteria: algorithm convergence, solar tracking throughout the duration of the measurement, and a root-mean-square (RMS) error below 1.5%.

2.3. TROPOMI. *2.3.1. CO Column Retrievals.* TROPOMI[47] is a polar-orbiting instrument that typically flies over the western U.S. between 20:00 and 22:00 UTC, or about 12:00−14:00 local time for the Rabbit Foot fire (11:00−13:00 local time for the Watson Creek fire). These local sampling times tend to fall before the typical peak fire activity at 21/22 and +2/+3 UTC in the western U.S. (e.g., Wiggins et al.[48]). The TROPOMI grating spectrometer measures solar spectra reflected by the Earth's surface in the UV−vis (270−500 nm), near-IR (675−775 nm), and SWIR (2305−2385 nm) spectral bands. Measured atmospheric trace gases included nitrogen dioxide (NO_2[49]), formaldehyde (HCHO[50]), nitrous acid (HONO[11]) CO, and CH_4.[27,28] The TROPOMI CO data product is derived from the SWIR measurements deploying the Shortwave Infrared CO Retrieval (SICOR) developed for the European Space Agency's (ESA) operational processing of TROPOMI data.[26] The algorithm is a multiscattering code that retrieves effective parameters describing the cloud contamination of the measurement (cloud height, cloud optical thickness) simultaneously with the trace gas columns. Hence, the total column averaging kernels (AVKs) supplied for individual retrievals reflect the loss of sensitivity of the retrieval under cloudy atmospheric conditions.

TROPOMI provides daily global coverage and, compared to older satellites, an improved spatial resolution up to 7.0 × 7.0 km^2 in the SWIR in 2018 (updated to 5.5 × 7.0 km^2 in August 2019). Data from TROPOMI has been used already to constrain daily emissions estimates of trace gases such as NO_x[51] and smaller point sources of pollution (e.g., Beirle et al.;[51] Theys et al.;[11] Jin et al.[34]). In most cases, TROPOMI was not measured in a nadir geometry, which led to pixel size deviations from the maximum 7.0 × 7.0 km^2 resolution, and is addressed in Section 3.1.

For this study, we use both the currently available TROPOMI CO dataset (Version 1.02.02 for the applicable orbits in 2018[52]) and the preoperational TROPOMI CO dataset developed by SRON The Netherlands Institute for Space Research, which includes features and improvements planned for ESA's future operational dataset.[10,53] The forward calculation of the operational dataset is based on the HITRAN

https://doi.org/10.1021/acsearthspacechem.2c00048
ACS Earth Space Chem. 2022, 6, 1799−1812

2008[54] database with an updated water vapor cross section.[55] The preoperational dataset uses the Scientific Exploitation of Operational Missions−Improved Atmospheric Spectroscopy Databases (SEOM-IAS) database developed for the TROPOMI mission (https://zenodo.org/record/1009122#.Yg_BxC-B1eM). Borsdorff et al.[10] showed that by using SEOM-IAS instead of HITRAN 2008 for the TROPOMI CO retrieval, a better spectral fit and a lower bias with TCCON and the Copernicus Atmospheric Monitoring Service−Integrated Forecasting System (CAMS-IFS) can be achieved. The SEOM-IAS is also used for the operational processing; however, the orbits used in this study were not yet reprocessed. More details about the operational product for CO are given in the algorithm theoretical baseline document (ATBD[27]) and user manual.[56] The two datasets are filtered for clear-sky and moderate cloud conditions using the quality assurance value ("qa_value") for each ground pixel (qa_value > 0.5[27]). Furthermore, the CO VCDs are corrected for stripe noise following the approach described by Borsdorff et al.[10]

In the UV regime, challenges arise with smoke plumes being optically thick, and measurements from the satellite and aircraft cannot be directly compared due to differences in the air mass factors (AMF), the weighted average photon path through the plume.[11] However, in the IR, we expect smoke masking to be much less of an issue (as is further corroborated in Section 3.6), enabling a more direct comparison of VCDs from both platforms.

2.3.2. CO Column Averaging Kernels. The TROPOMI CO retrieval algorithm scales a vertical concentration profile of CO to achieve a good fit between the simulation and measurement.[57] This makes use of a priori information on the CO vertical distribution taken from the TM5 model.[58] However, the actual vertical distribution may differ significantly from the a priori, and for data interpretation, the algorithm calculates a CO column AVK for each ground pixel. The AVK characterizes the vertical sensitivity of the retrieval and the relative contribution of the measurement and a priori at each altitude.[59] Figure 1 in Borsdorff et al.[9] shows example cases for total column averaging kernels under clear-sky and cloudy conditions. The lowermost value of the AVK representative for the ground level for clear-sky conditions is, in general, higher than 0.8, indicating good sensitivity for CO. This value is reduced for cloud-contaminated measurements due to shielding and scattering of light by clouds in the observation geometry of the satellite.

In this study, we use the AVK supplied with the TROPOMI CO measurements to correct for the smoothing error of the retrieval by assuming that the vertical CO concentration profile measured by the aircraft is an estimate of the truth and representative of the whole plume. We extend the aircraft profile above the maximal flight height (5−6 km) with the a priori information used in the TROPOMI retrieval. The AVK correction is done as given in eq 1

$$\mathrm{AVK}_{\mathrm{corr}} = \frac{\int_0^z \mathrm{AVK}(z)N(z)\mathrm{d}z}{\int_0^z N(z)\mathrm{d}z} \tag{1}$$

where $\mathrm{AVK}(z)$ is the AVK value at some height z, $N(z)$ is the CO concentration at height z, and $\mathrm{d}z$ is the height of the altitude bin where the AVK is calculated, which is defined by the TROPOMI radiative transfer vertical grid. When a profile measurement from the aircraft is available to characterize $N(z)$, the measured CO concentration is used in place of the CO and grid from TM5. Outside the measurement range of the aircraft, a priori data from TM5 is used. The resulting corrected VCD, $\mathrm{VCD}_{\mathrm{corr}}$, for TROPOMI, is scaled inversely by $\mathrm{AVK}_{\mathrm{corr}}$ such that $\mathrm{VCD}_{\mathrm{corr}} = \mathrm{VCD}/\mathrm{AVK}_{\mathrm{corr}}$.

2.4. Bridging Geospatial Sampling Scales. Comparisons between measurements of a suborbital aircraft platform and satellites require reconciliation of their respective spatial sampling scales. CU AirSOF averages spectra every 4 s, whereas TROPOMI surveys the wildfire up to twice during the day if the fire is at the edge of an orbit scan. We define integrated CO differential VCDs (dVCDs) to bridge the spatial sampling scales, where the dVCD has been background-corrected. In cases where TROPOMI measurements can be sampled along the aircraft transect, we define that transect as the line integral path according to eq 2, where s is the distance along the transect.

$$\int_0^s \mathrm{dVCD}\,\mathrm{d}s = \int_0^s (\mathrm{VCD} - \mathrm{VCD}_{\mathrm{bkgd}})\mathrm{d}s \tag{2}$$

By integrating, we average CO along a cross section of the plume; assuming the air mass is the same, these values should be comparable over the fine and coarse sampling scales of CU AirSOF and TROPOMI, respectively.

For the aircraft, the background is sampled on either side of the plume and linearly interpolated across the flight transect. Thus, the background may be variable across multiple transects. This analysis becomes more complex for the satellite when the plume structure and surrounding scene are not well constrained. The aircraft, sampling on a much finer spatial scale, can resolve smaller discrepancies in background air versus the biomass plume, whereas the satellite could fail to resolve the plume edge depending on the ground pixel size. Thus, for cases where horizontal plume transect shapes are not the same, we define a transaction line near-parallel to the flight transect and draw the line far into the air mass outside of the plume. The CO column along the transaction lines is assumed to have a Gaussian distribution, $G(x)$. Additionally, the background on either side of the transaction line can vary; thus, the extracted VCDs along the transaction line can be expressed as $H_0 + H_1x + A_0G(x)$, where $H_0 + H_1x$ represents the background correction along the line. The corresponding error due to background variability is described further in Section 3.5.

2.5. Bridging Temporal Scales. In addition to the integration approach, some case studies presented in this paper did not have near-synchronous measurement times; however, these cases could still be analyzed after correcting for the time elapsed from smoke emissions from the fire source to the sampled location of the aircraft and TROPOMI. The transport time was estimated using the Lagrangian particle dispersion model FLEXPART coupled with the Weather Research and Forecasting (WRF) model (FLEXPART-WRF[38]) following the method described in Theys et al.[11] Briefly, particles were released and advected from each fire location using emission strength and plume injection height from the Global Fire Assimilation System[60] and meteorological data from WRF (using meteorological fields from the European Centre for Medium-Range Weather Forecasts up to a 2.5 km resolution). The model output was binned into different age classes defined as the time elapsed since the release of the particles. The plume age was then retrieved at the aircraft coordinates and for every TROPOMI pixel center.

https://doi.org/10.1021/acsearthspacechem.2c00048
ACS Earth Space Chem. 2022, 6, 1799−1812

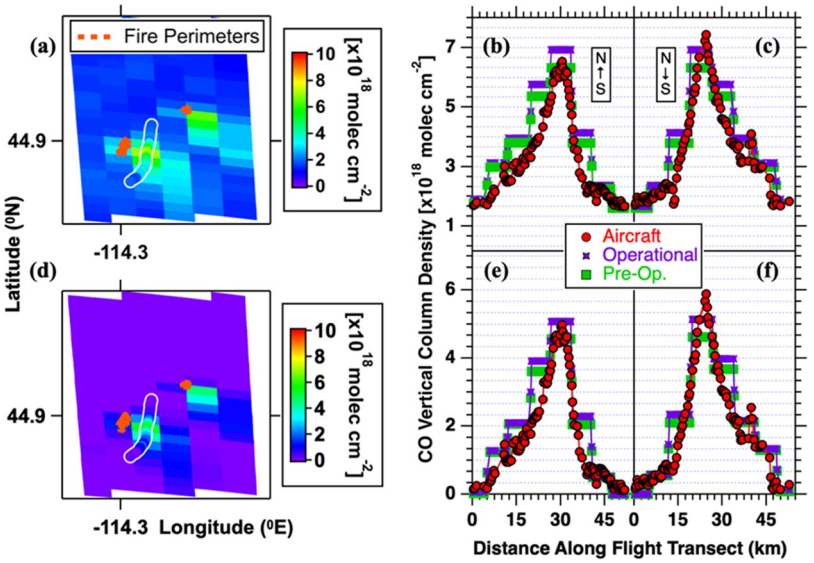

Figure 2. Top row: (a) CO VCDs as observed by TROPOMI during the 15 August 2018 Rabbit Foot fire (during RF13). (b, c) Aircraft measurements of the midpoint VCD (red circles) plotted along a sampling axis. TROPOMI data (operational: purple crosses, preoperational: green squares) are extracted along the aircraft flight track and plotted along the same distance axis. Bottom row: (d–f) same as the top row, except background corrections have been applied by averaging at the start and stop of each measurement. Note that with background subtraction applied, and the direction of the winds being northwesterly, the Goldstone fire (northeast of the flight transect) is not actively contributing to the Rabbit Foot fire biomass burning plume and is ignored.

Finally, the pixels with the same plume age as the aircraft, either upwind or downwind, were outlined and corrected for transport time (Theys et al.[11]). Errors could persist as several fires were found to strengthen rapidly over tens of minutes when sampled back-to-back by CU AirSOF and must be considered before comparing integrated dVCDs between each platform.

2.6. Selection of Case Studies. For this study, seven RFs are well suited for comparison with the TROPOMI CO data products, as detailed in Table 1. Given that TROPOMI passes through the scenes once during the day between 20:00 and 22:00 UTC (11/12:00 and 13/14:00 local time), we select cases with time differences of an hour or less between TROPOMI and CU AirSOF. The criterion of an hour maximum time difference was to ensure that CO columns were compared with minimal possibility of mixing with recirculation of aged air from wildfire smoke. Larger time deltas come with the risk of rapidly evolving fire strength in time, which could introduce significant error if the satellite scene has changed significantly compared to when the aircraft made a measurement. With this constraint, we then focus on case studies with well-defined plumes, and clear, unpolluted CO backgrounds next to the plumes. In more heterogeneous scenes, such as RF15, the analysis can still be performed using the transaction lines discussed in Section 2.5. Additional case studies are described in Text S3.

2.7. Radiative Transfer Simulations. The Monte Carlo Atmospheric Radiative Transfer Inversion Model version 3 (McArtim3[61]) program was used to understand the effect of aerosol particles on the transmission of light through a biomass burning plume. Full details of the simulations are given in the Supporting Information (see Text S4). In brief, an aerosol plume with a predefined IR aerosol optical depth (AOD) was simulated at a plume peak of 2.0 km above sea level (kmsl), assuming the ground is at 1.0 kmsl, and distributed vertically using a Gaussian function with a full width at half-maximum of 0.5 km. McArtim3 outputs are used to calculate the Box Air Mass Factor (BoxAMF), which quantifies the sensitivity of the photon path to changes in concentrations for a modeled altitude bin. The model was run at a fine altitude grid (0.05 km layers) in the lowest 3.0 km to resolve detailed information on the BoxAMF and was then run at a coarser grid (ca. 0.5–1.0 km layers) to the top of the atmosphere. Simulations were run in the UV (355 nm), visible (455 nm), and SWIR (2337.5 nm), with absorbers appropriate for each window (see Table S2).

3. RESULTS AND DISCUSSION

3.1. RF13 Case Study. Figure 2a shows the satellite scan of the Rabbit Foot fire during RF13 on 15 August 2018. Aircraft data for two underpasses with minimal temporal differences (<10 min) to the satellite are plotted in Figure 2b,c with the extracted satellite data along the flight track. CU AirSOF captures some fire strengthening across the two underpasses, but the plume shape is relatively unchanged and peaks at the same distance along the flight track. The aircraft captures peak values of 7.5 × 10^{18} molec cm^{-2} of CO, and the satellite detects 7.0 × 10^{18} molec cm^{-2} of CO at the same location, both without background subtraction. This 7% difference in the CO VCD measurement between each platform suggests that TROPOMI is also measuring the entire CO column since CU AirSOF captures nearly 100% of the total plume CO (see Table 1). The preoperational TROPOMI data does show lower CO VCDs and is in better agreement with aircraft data from the fourth underpass. At the sub-pixel scale, CU AirSOF captures stronger variability with individual measurements averaged every 4 s. TROPOMI also captures this variability at a coarser scale. In plume edges, this could lead to larger uncertainties in the retrieved CO.

The background offset becomes straightforward when the measurement platforms have good spatial and temporal alignment. Figure 2b,c shows nearly identical CO VCDs at

https://doi.org/10.1021/acsearthspacechem.2c00048
ACS Earth Space Chem. 2022, 6, 1799–1812

the plume ends of each measurement transect (exact values in Table S3). Thus, the average of the two regions outside the plume can be used to derive a background-corrected CO dVCD product for the entire scene, as shown in Figure 2d–f. The TROPOMI pixel sizes are large for the RF13 case study (shown in Table S3); however, we hypothesize that since the longer dimension of the TROPOMI pixels is aligned with the mean direction of the wind field, this is not a limitation on interpreting the dataset. The minor axis was parallel with the aircraft transect, and longitudinal heterogeneity of the CO VCDs could be assessed by both the satellite and aircraft into background.

Finally, Figure 3 shows the pixel to aircraft correlation of the operational CO VCD without background subtraction.

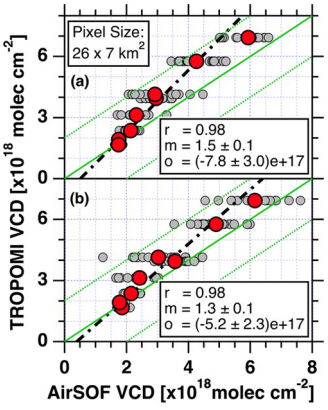

Figure 3. Raw TROPOMI versus CU AirSOF CO VCDs for CO extracted along the aircraft flight track. RF13 for (a) PUN_C-04 and (b) PUN_C-05. Red points are averaged aircraft measurements over each TROPOMI pixel, and gray points display the variability in aircraft measurements for each pixel. Also plotted in green are 1:1, 2:1, and 1:2 lines. The best fit line (dashed black line) using a nonlinear orthogonal distance regression is shown.

Generally, the satellite sees slightly higher values compared to CU AirSOF, especially outside of the maximum CO VCDs in the plume center. It is interesting to note that larger deviations are observed for mid-level CO VCDs, and could be related to the pixel resolution of TROPOMI, where the mismatch between spatial scales probed is relatively more important in heterogeneous scenes near the plume boundary. The slope in the fifth underpass in Figure 3b is 1.3, suggesting operational TROPOMI data was, on average, 30% higher than CU AirSOF data during this time-aligned underpass. The fourth underpass, shown in Figure 3a, occurs ∼15 min prior to the TROPOMI overpass and had a slope of 1.5, which is indicative of fast wildfire intensification over tens of minutes. When TROPOMI aligns in time with CU AirSOF, the CO VCD agreement improved by ∼20%.

3.2. Challenges of the RF11 Case Study. *3.2.1. Time Alignment with FLEXPART.* CU AirSOF was sampling the Rabbit Foot fire around 20:00 UTC on 12 August 2018 during RF11 and TROPOMI conducted its overpass at 20:45 UTC. A correction is needed to identify the satellite pixels corresponding to the CU AirSOF measurement. FLEXPART indicates the range of pixels in Figure 4, and transaction lines are drawn to sample TROPOMI CO VCDs through different transects, each corresponding to a slightly different plume age. The bolded transaction line from Figure 4 was chosen to integrate the CO dVCD. The error from choosing different lines, in an

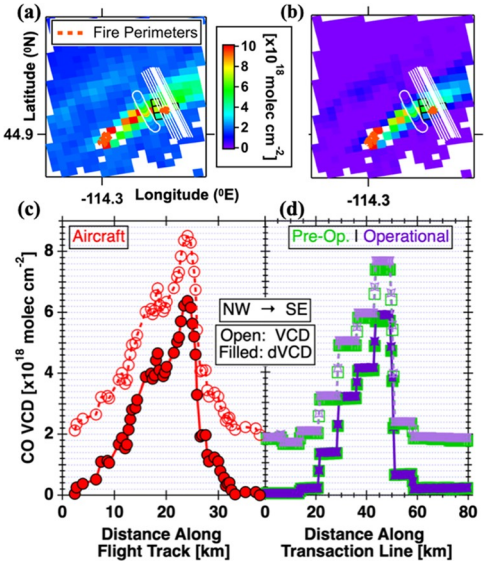

Figure 4. Top row: (a) CO VCDs as seen by TROPOMI, with dVCDs shown in (b). Overlaid in filled circles are the CU AirSOF CO VCDs measured before the satellite overpass. Black pixel outlines indicate the range of TROPOMI data to be sampled. (c) Aircraft data for a plume underpass during RF11. (d) Extracted TROPOMI CO measurements along the bolded transaction line from (a, b).

attempt to characterize FLEXPART plume age errors, is explored in Section 3.5. Additional case studies requiring time alignment of CU AirSOF and TROPOMI data are explored in the Supporting Information.

3.2.2. Background Observations between Sampling Scales. Due to the FLEXPART correction needed to compare the aircraft to the satellite, transaction lines are drawn in Figure 4a,b approximately parallel to the flight track and extend far into the background. For a homogeneous scene such as RF13, this variability is expected to be low. For RF11, however, after background correction, Figure 4b reveals some enhancements north of the Rabbit Foot fire that are not removed with the local correction.

After the background correction is applied, the wildfire plume comparison can be made. Figure 4c shows CO VCDs and dVCDs from the CU AirSOF underpass, and Figure 4d shows the extracted information downwind using the TROPOMI CO datasets. Note that the distance sampling scales are no longer identical since lateral dispersion has occurred downwind, which emphasizes the importance of a carefully calculated background. With the FLEXPART corrections, the backgrounds differ for the aircraft and satellite, measured at $\sim 2.1 \times 10^{18}$ and 1.8×10^{18} molec cm^{-2} of CO (1.7×10^{18} molec cm^{-2} preoperational), respectively. After correcting for the background, at the plume peak, both platforms measure $\sim 6 \times 10^{18}$ molec cm^{-2} of CO. However, the plume widths measured by each platform differ from background to background. The width is ∼30 km from aircraft measurements, whereas the width from the satellite is ∼40 km. The use of transaction lines and FLEXPART assist to apply a consistent background correction across spatial and temporal scales for each platform.

3.3. Leveraging Profile Shape Information. Recall from Section 2.3.2 that the true vertical distribution of CO is known from aircraft measurements. Under the assumption that it is representative of the full domain of the plume, the smoothing

https://doi.org/10.1021/acsearthspacechem.2c00048
ACS Earth Space Chem. 2022, 6, 1799−1812

error of the column retrieved by TROPOMI can be corrected. Figure 5a shows the in situ aircraft information during RF11,

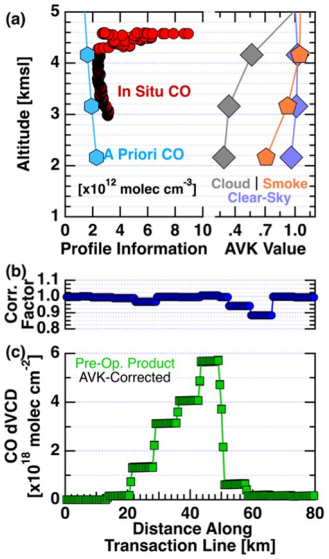

Figure 5. (a) From left to right: Vertical profiles of the in situ aircraft measurements during RF11, a priori CO profile used in the TROPOMI retrieval algorithm, and extracted preoperational column averaging kernels for a cloudy, plume edge (or clear), and smoke-filled pixel. (b) AVK correction factor derived from the top row of information. (c) Preoperational satellite dVCD (green boxes) and AVK-corrected dVCD (black boxes).

profile information, and CO column AVKs. When the pixel is cloud-contaminated, the AVK falls to ∼0.3 near the surface. When applying eq 1, Figure 5b shows the calculated AVK correction factor at each point along the satellite transaction line chosen for comparison in RF11. In general, the pixel AVK is well constrained by the a priori information on the CO profile except for the southern-most edge of the plume. The correction factor, however, tended to be near unity, and in near-background conditions, contributions to the final integration value would be small.

AVK correction factors are calculated for the remaining research flights in Figure S6. In general, the AVK correction factor did not correct the TROPOMI VCD more than 20% across all cases, and these larger corrections typically occurred along the plume edges or backgrounds. Only RF22 was substantially impacted by the in situ profile information near the plume peak, and a smaller total integrated CO dVCD was calculated.

3.4. Integrated CO dVCDs in Wildfire Smoke. After all corrections have been made to resolve spatial and temporal differences between each platform, the CO dVCDs were integrated along each aircraft transect and transaction line and are illustrated in Figure 6. Cases that required a FLEXPART correction are identified and the timestamp for each measurement is labeled along the horizontal axis. RF13 has the most straightforward analysis, and the integrated result for the satellite was higher by +30% for the operational dataset (+22% preoperational). The preoperational dataset improved the comparison for RF13. RF15 highlights the strength of using a longer transaction line to appropriately background-correct the raw VCDs in both satellite products. The comparison to PUN_C-02, which occurred during the TROPOMI overpass, only differed by +4.9% (+3.2% preoperational). FLEXPART

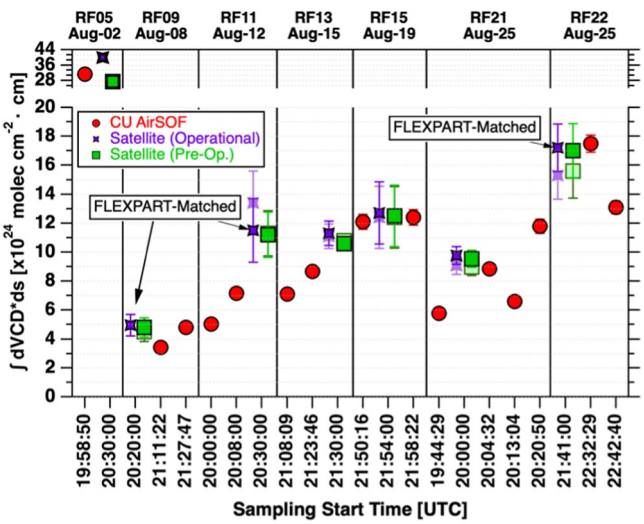

Figure 6. Summary of the integrated dVCDs for all case studies for CU AirSOF underpasses (red circles), operational TROPOMI data (purple crosses), and preoperational TROPOMI data (green squares). Lighter-colored satellite markers perform the integration using the AVK correction factor on the dVCD from Figures 5 (and S6) to correct for the in situ profile shape measured during BB-FLUX.

was most useful in RF22 where the integrated CO dVCDs relative to aircraft transect PUN_C-01 differed only by −1.6% (−2.7%). In general, the integrated CO dVCDs were found to be higher than the aircraft even after resolving for the spatial and temporal differences. The preoperational dataset was found to reduce this high relative difference.

Integration results were comparable within 68% for RF05, but the difference likely derives from the length of the integration and heterogeneity measured by the aircraft over a substantial sampling time. RF11 resulted in a poor comparison likely due to rapidly strengthening emissions on the order of minutes between transects, as revealed by CU AirSOF. Thus, accurate assignment of the plume age at the aircraft and satellite is exceedingly important to make the best comparison. When taken to a global scale, this result also highlights the importance of fast temporal variability of wildfires.

3.5. Error Budget. *3.5.1. Error Calculations.* Components of the error bars are reported in Table 2 for each measurement platform while considering both instrument and comparison errors. As shown in Kille et al.,[22] CU AirSOF errors are limited to systematic uncertainties due to the CO cross section (2.6% uncertainty) and random sampling errors (5.5% uncertainty), where the latter is reduced by scaling the error by the inverse square root of the number of measurements in the background air. For the comparison errors, the background uncertainty was calculated by comparing the mean background CO VCDs on the plume edges relative to the mean CO VCD enhancement. This error generally contributed a small amount to the total quadrature sum, averaging ∼1.7% for all case studies. This indicated that CU AirSOF measures comparable backgrounds on either side of the plume and generally does not limit the total error (with exception of RF15). Generally, the geospatial position error of the aircraft is small with latitude and longitude errors of 9×10^{-6} and 1.2×10^{-5} degrees, respectively, with an average error contribution of ∼0.5% or smaller. Overall, the aircraft measurement is well constrained, in part owing to the better spatial resolution to characterize backgrounds on either side of the plume.

https://doi.org/10.1021/acsearthspacechem.2c00048
ACS Earth Space Chem. 2022, 6, 1799−1812

Table 2. Error Budget Analysis for CU AirSOF and TROPOMI for All Research Flight Case Studies Integration Values Following Figure 6[a]

			case study and corresponding percent error on the integration						
platform	error type	error source	RF05	RF09	RF11	RF13	RF15	RF21	RF22
aircraft	instrument	systematic (XS error)	2.6	2.6	2.6	2.6	2.6	2.6	2.6
		random variability	0.4	1.0	1.2	0.7	1.4	1.7	1.9
	comparison	background correction[b]	0.6	1.9	2.4	0.8	3.1	2.7	0.7
		average distance	0.2	0.3	0.0	0.3	0.3	0.5	0.2
		average total integral error	2.7	3.4	3.7	2.8	4.3	4.1	3.3
satellite operational	instrument	systematic uncertainty	1.9	4.8	4.3	1.9	3.1	5.6	3.8
		null space (AVK correction)	0.1	0.1	14	0.3	0.2	2.7	1.6
	comparison	background variability[c]	11	2.5	3.5	7.2	8.4	1.3	3.0
		FLEXPART line error		14	13		14	1.1	8.0
		total integral error	11	15	19	7.5	17	6.4	9.5
satellite preop.	instrument	systematic uncertainty	2.8	2.5	4.3	1.9	3.1	5.6	3.8
		null space (AVK correction)	0.1	0.1	3.5	1.4	0.0	1.9	4.8
	comparison	background variability[c]	8.7	2.5	3.7	2.4	8.3	1.5	2.8
		FLEXPART line error		14	12		15	1.1	8.2
		total integral error	9.1	14	14	3.4	17	6.2	11

[a]All errors are expressed as percentages. [b]Background correction on SOF performed by comparing plume edge CO to mean plume-enhanced CO. [c]Background variability assessed by comparing mean CO outside plume in neighboring pixels relative to mean enhancement.

Our comparison method using TROPOMI CO is affected by instrument errors, including systematic uncertainty and the AVK correction (null space), and comparison errors due to background variability and the FLEXPART correction. First, both the operational and preoperational datasets include the standard error of the vertically integrated CO propagated along the integration track as a systematic uncertainty, ranging from 1.9 to 5.6%. For the AVK, when information on the true profile shape is unavailable, no correction is made on the VCD. These errors are generally small, where the AVK is more representative of a clear-sky environment; however, variability can peak as high as 14%.

Background variability is calculated by looking at the variation of the background outside the plume edge near the satellite integration line. RF05 (see Figure S1a) had the highest background variability at 11% for the operational product (8.7% preoperational) and RF21 had the lowest background variability at 1.3% for the operational product (1.5% preoperational). Transaction lines can also be used to assess the error of our dVCD calculation. The standard deviation of neighboring transaction line integration values is compared to the mean of the selected range to represent any transport errors due to FLEXPART. This also characterizes a discretization error for the sampled pixels, but more data would be needed to separate this further. In total, an error range of 1.1−14% in the operational dataset (15% preoperational), was calculated using the transaction lines. RF13 did not consider a transport error since transaction lines were not necessary for the integration comparison. To get a total integration error for all cases, a quadrature sum is performed, assuming that any errors labeled as systematic (or precision) in the satellite dataset cannot be individually attributed to a positive or negative offset to the VCD.

3.5.2. Bias Assessment. Without considering geospatial and FLEXPART emission time corrections, the integrated dVCD difference of TROPOMI CO relative to CU AirSOF was found to be +36 and +27% for the operational and preoperational datasets, respectively (+36 and +23% when leveraging the AVK correction), as shown in Table 3 (see Table S3 for exact values). The 95% confidence intervals (CI) differ substantially from the mean, indicating this relative difference is significant. After removing an outlier from the RF11 case study, this comparison improves to +30% operational and +21% preoperational (+26 and +16% with the AVKs, respectively), while remaining statistically significant. A consistent finding is that the preoperational dataset improves the high relative difference of TROPOMI and is further improved when using the AVK correction.

Table 3. Bias Assessment of TROPOMI Relative to Aircraft[a,b]

description	number of data points	operational satellite relative difference	preop. satellite relative difference
all integrals	15	36 ± 21 [32]	27 ± 20 [22]
using AVK		36 ± 27 [28]	23 ± 21 [18]
remove outlier[c]	14	30 ± 17 [31]	21 ± 16 [15]
using AVK		26 ± 19 [23]	16 ± 16 [10]
quality assured[d]	10	16 ± 15 [7.7]	13 ± 15 [5.6]
using AVK		10 ± 15 [2.8]	7.2 ± 15 [2.8]

[a]Error bounds are expressed as average ± 95% confidence interval [median] (%). [b]TROPOMI Mission Requirements from Veefkind et al.:[47] 10% precision, 15% accuracy for a single pixel; ∼8% over ∼4 integrated pixels. [c]Removes 1 transect from RF11. [d]Requires FLEXPART and/or geospatial alignment, RF05, RF11, RF13 PUN_C-04, and RF21 PUN_C-04 are removed from this analysis.

Quality assurance steps were taken to further constrain the error bounds. These steps required that the platforms were aligned temporally and geospatially, using FLEXPART, if necessary, and that outliers were removed. In total, 10 integrals are left to evaluate. When using the AVKs, the comparison difference relative to the aircraft is reduced to +10% operational and +7.2% preoperational. While a statistically insignificant result, the preoperational dataset improves the analysis, which is a consistent finding. With respect to the 10% precision and 15% accuracy requirements,[47] TROPOMI CO, with efforts to reduce the comparison bias through quality assurance steps, is within the operational design requirements for biomass burning plumes.

https://doi.org/10.1021/acsearthspacechem.2c00048
ACS Earth Space Chem. 2022, 6, 1799−1812

Additionally, CU AirSOF case study errors can be used to conclude that atmospheric variability on the subsatellite pixel scale remains a significant, yet statistical, source of uncertainty. Integrated CO dVCDs varied on average by 2.4×10^{24} molec cm^{-2}·cm (28% on average, full range: 6.6−64%), which was lower than any integrated CO dVCD measured by the satellite. Atmospheric variability with respect to the satellite is significant with respect to the fundamental sampling challenge. The preoperational dataset helped reduce the comparison bias for the study, which is in line with the findings of Borsdorff et al.,[9] showing that the high bias of TROPOMI CO with TCCON is reduced from 6.2 ppb (operational processing) to 3 ppb (preoperational). As shown here, a small positive relative difference remains in comparison with the TCCON reference measurements, perhaps due to aerosol multiple scattering in optically thick wildfire smoke. This effect is explored in further detail in Section 3.6. Small contributions to the bias are expected in wildfire smoke but cannot be individually attributed like what was shown for CU AirSOF. Thus, it is expected that part of the difference is due to heterogeneity within the 3-D measurement volume of the wildfire plume.

3.6. Radiative Transfer in Optically Thick Plumes. Figure 7 shows the resulting McArtim3 calculations for these spectral regimes. The top row shows the calculated BoxAMFs, and the bottom row illustrates an ideal profile shape by convolving a unit-area Gaussian aerosol plume that was used to model aerosol extinction in McArtim3. For AOD_{355} greater than 1.0, the BoxAMF falls to zero quickly in the lowest 1.5 kmsl. Some information can be leveraged below the plume for AOD_{355} less than 1.0 and more so in the visible, however, low aerosol loads, where AOD_{355} = 0.05 would be needed to attain BoxAMFs near 1.0 at plume peak in the UV. Figure 7c,f shows the equivalent information for the SWIR regime. Upon comparison, the peak BoxAMF values occur at the plume peak of 2.0 km in both cases, however, the behavior below the plume is different across the spectral regimes. At low aerosol loads, where the original AOD_{355} is less than 1.0, effects of aerosol extinction at all regimes are minimized as sensitivity is retained throughout the vertical extent of the atmosphere. Interestingly, for all $AOD_{2337.5}$, the BoxAMFs are geometric (values > ∼2.1), which is indicative of a photon traveling through the plume, reflecting off the surface, and traveling through the plume a second time before arriving at the TROPOMI detector.

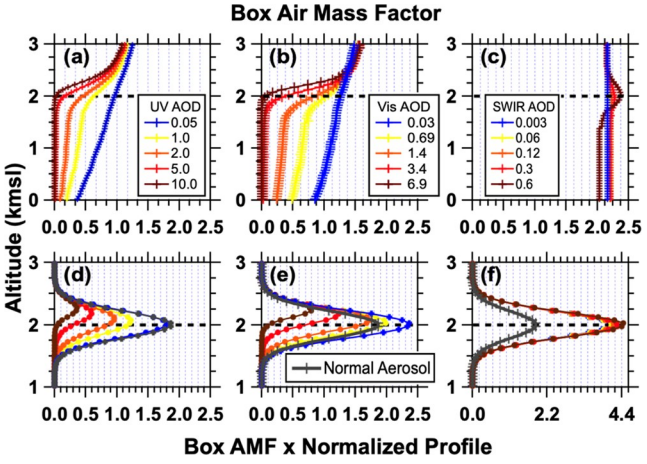

Figure 7. (a) UV, (b) visible, and (c) SWIR box air mass factors simulated for a Gaussian-distributed aerosol profile (gray trace in (d−f)) following the fit parameters in Table S2. These calculations are performed for a nadir viewing satellite under idealized geometries. Selected (d) UV, (e) visible, and (f) SWIR box air mass factors multiplied by a unit-area Gaussian to illustrate the effect of profile shape on the sensitivity of the retrieval.

AMFs, shown in Table 4, were calculated for the UV, visible, and SWIR regimes by integrating the BoxAMFs over the vertical extent of the model grid. As was found in Theys et al.,[11] at AOD_{355} greater than 2.0, the AMF falls off below 0.3 due to smoke masking, and the measured TROPOMI column would require an ∼6× correction on the SCD to convert to a VCD. The SWIR AMF exceeded 2.16 for all $AOD_{2337.5}$ and a surface albedo of 0.10. As discussed in Landgraf et al.,[27] the TROPOMI SWIR retrieval struggles in the presence of clouds. However, these RTM calculations suggest at modest surface albedos near 0.1, TROPOMI is capable of sensing CO in thick wildfire plumes that, while optically dense in the UV−vis, are optically thinner in the SWIR.

Figure 8 shows the results of the albedo sensitivity studies performed for the SWIR. In the absence of surface reflectivity, shown in Figure 8a,e, the SWIR behaves similarly to the UV case study shown previously where photon sensitivity falls to zero below the plume peak of 2.0 km. This suggests that photon backscatter in the aerosol plume is responsible for the increased BoxAMF values rather than scattering due to albedo. As the surface albedo was increased to 0.05 in panels (b) and (f), sensitivity below the plume peak was reestablished for all $AOD_{2337.5}$. For example, for $AOD_{2337.5}$ = 0.6, the BoxAMF below the plume was ∼1.6 and could vary as high as ∼2.2 for a surface albedo of 0.05. From Table 4, even with no albedo in the SWIR, adding in the aerosol such that $AOD_{2337.5}$ = 0.6 brings the AMF within 20% of the AMF in the same case ran with a surface albedo of 0.05. Thus, aerosol backscatter accounts for a significant number of photons returned to the detector with additional contributions due to increases in surface reflectivity.

Values greater than 2.15 (geometric photon paths) indicate that the path length has increased over the geometric value. Since albedo does not account for this effect, aerosol multiple scattering, e.g., in thick wildfire smoke, could explain this effect. We hypothesize that this effect accounts for a small percentage of the disagreement between the platforms. From Figure 8b, for an $AOD_{2337.5}$ of 0.12 or less, the BoxAMF ranges from ∼2.16 to ∼2.35 at the 2.0 km plume peak and results in a near-constant AMF calculation. Then, up to ∼3.6% variability is seen between the cases where $AOD_{2337.5}$ exceeds 0.12, which suggests that multiple scattering is occurring inside the plumes and would lead to higher absolute VCDs seen by TROPOMI. Hence, a CO retrieval approach that would not account for multiple scattering on aerosols in the plume would overestimate the VCD. The TROPOMI CO retrieval uses a multiscattering forward calculation in the retrieval accounting for this effect; however, a more complex model may be needed to account for scattering by aerosols in optically thick wildfire smoke.

4. CONCLUSIONS AND OUTLOOK

Suborbital measurements of CO VCDs from CU AirSOF were used to evaluate the performance of the TROPOMI operational and preoperational CO data products in smoke plumes during the 2018 Western U.S. wildfire season. CU AirSOF and TROPOMI both measure CO VCDs, but CU AirSOF

https://doi.org/10.1021/acsearthspacechem.2c00048
ACS Earth Space Chem. 2022, 6, 1799−1812

Table 4. Calculated AMFs from McArtim3 Following TROPOMI Geometry (SA Stands for Surface Albedo)[a]

	spectral regime AMFs					
	UV (355 nm)	vis (455 nm)	SWIR (2337.5 nm)			
UV AOD case study[b,c]	SA = 0.05	SA = 0.05	SA = 0.0	SA = 0.05	SA = 0.10	SA = 0.15
0.05	0.96	1.27	1.09	2.15	2.16	2.15
0.10	0.93	1.23	1.20	2.15	2.16	2.16
0.20	0.88	1.20	1.30	2.15	2.16	2.16
0.50	0.78	1.12	1.44	2.16	2.17	2.18
1.0	0.65	1.03	1.52	2.16	2.19	2.19
2.0	0.49	0.85	1.57	2.18	2.21	2.21
5.0	0.25	0.50	1.72	2.21	2.25	2.29
10.0	0.13	0.27	1.85	2.21	2.29	2.34

[a]UV AODs are scaled and follow the accompanying sequence: ..., 0.60. Full details of this calculation are provided in Text S4. [b]Visible AODs: 0.03, 0.07, 0.14, 0.34, 0.69, 1.38, 3.44, 6.89. [c]SWIR AODs: 0.003, 0.006, 0.01, 0.03, 0.06, 0.12, 0.30, 0.60.

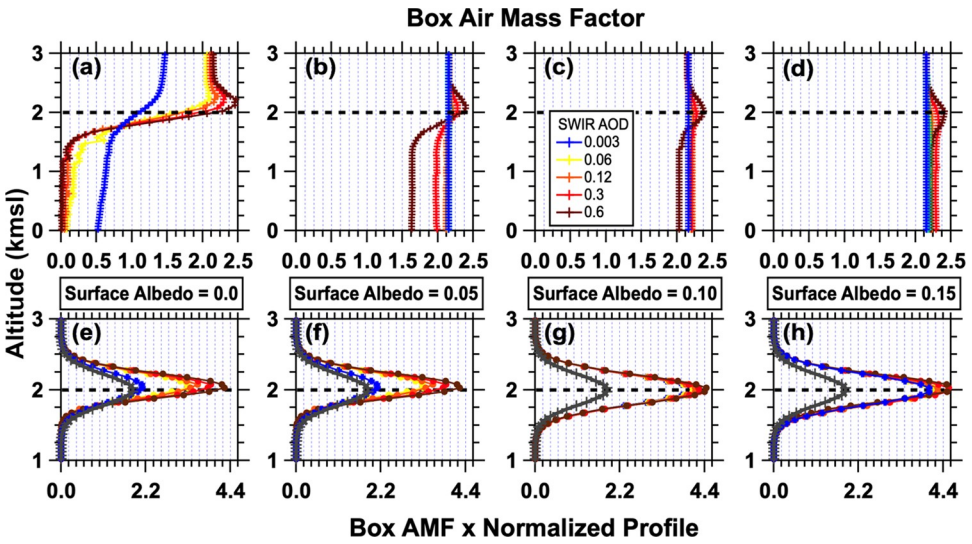

Figure 8. Albedo sensitivity study for the SWIR spectral regime. Surface albedos from 0.0 to 0.15 were tested. (a–d) BoxAMFs and (e–h) normalized profile shapes to the aerosol plume (gray trace).

conducts measurements at finer spatial resolution (few 100 m) in an upward-looking geometry that complements the satellite nadir view. Advantages of deploying CU AirSOF include the ability to actively deal with the sampling challenge by integrating small-scale variations in CO concentrations both vertically and horizontally across the entire plume cross section (every 10–30 min), the ability to better access background CO columns adjacent to the plumes, and the ability to characterize CO VCD variations within satellite ground pixels. Such access over the entire plume volume is a prerequisite to approximating the temporal (once or twice daily) and spatial scales probed by TROPOMI. The key results from the comparisons are as follows:

- FLEXPART reduced the comparison bias between CU AirSOF and TROPOMI CO measurements and revealed that the preoperational satellite dataset improved the high bias to +7.2% after considering the AVK.
- The reduction of systematic high bias identified in this paper at high aerosol load is consistent with the findings of Borsdorff et al.[9] showing that deploying the SEOM-IAS cross sections in the preoperational retrieval reduces the bias with TCCON from ∼6.5% (operational) to 3.2% (preoperational). TCCON stations are located mainly in unpolluted remote areas, where CO VCDs and aerosol load are lower than in this study. A minor contribution to the high comparison difference (1–3%) is likely not caused by high aerosol load. An evaluation at TCCON sites near polluted regions is desirable.
- Radiative transfer modeling suggests that the TROPOMI CO retrieval is sensitive to CO measurements throughout the entire vertical extent of the wildfire plume. Total column measurements are possible even under the extreme case of high aerosol load within thick smoke plumes.
- Radiative transfer simulations indicate that multiple scattering typically is responsible for increasing satellite CO signals by 5–10% in thick smoke plumes; by contrast, smoke masking can reduce satellite signals of UV-absorbing gases by up to a factor 6 (600%) in thick smoke.
- The forward model of the TROPOMI CO retrieval accounts for multiple scattering on aerosols; however, it was designed to be applicable for global retrievals. Hence, future studies are needed to see if improvements can be made in wildfire smoke.

This study showed that CU AirSOF is a powerful tool to evaluate satellite measurements even under heterogeneous conditions and at high aerosol pollution typical of wildfire plumes. A simple, direct comparison of the measurements is

https://doi.org/10.1021/acsearthspacechem.2c00048
ACS Earth Space Chem. 2022, 6, 1799–1812

not possible in most cases since the strong temporal and spatial variability of CO in the wildfire plume needs to be accounted for. Future work would also include three-dimensional radiative transfer, which might be needed to resolve sub-pixel variability in radiative conditions. Globally, access to an aircraft may be limited or impossible, and this study confirmed for the first time that the TROPOMI CO product can be used to evaluate global wildfire emission fluxes with careful consideration taken for background corrections, ground pixel size, and atmospheric variability.

■ ASSOCIATED CONTENT

Supporting Information

The Supporting Information is available free of charge at https://pubs.acs.org/doi/10.1021/acsearthspacechem.2c00048.

Rationale for the integration approach to minimize comparison error between the aircraft and the satellite, flight codes used in Table 1, further details about BB-FLUX case studies, and radiative transfer calculations (PDF)

■ AUTHOR INFORMATION

Corresponding Author

Rainer Volkamer − *Department of Chemistry, University of Colorado Boulder, Boulder, Colorado 80309-0215, United States; Cooperative Institute for Research in Environmental Sciences, University of Colorado Boulder, Boulder, Colorado 80309-0216, United States; Department of Atmospheric and Oceanic Sciences, University of Colorado Boulder, Boulder, Colorado 80309-0311, United States;* orcid.org/0000-0002-0899-1369; Email: rainer.volkamer@colorado.edu

Authors

Jake P. Rowe − *Department of Chemistry, University of Colorado Boulder, Boulder, Colorado 80309-0215, United States; Cooperative Institute for Research in Environmental Sciences, University of Colorado Boulder, Boulder, Colorado 80309-0216, United States*

Kyle J. Zarzana − *Department of Chemistry, University of Colorado Boulder, Boulder, Colorado 80309-0215, United States;* orcid.org/0000-0003-1581-6419

Natalie Kille − *Department of Chemistry, University of Colorado Boulder, Boulder, Colorado 80309-0215, United States; Cooperative Institute for Research in Environmental Sciences, University of Colorado Boulder, Boulder, Colorado 80309-0216, United States; Department of Atmospheric and Oceanic Sciences, University of Colorado Boulder, Boulder, Colorado 80309-0311, United States;* Present Address: Institute of Energy and Climate Research: Troposphere (IEK-8), Forschungszentrum Jülich GmbH, Jülich 52425, Germany.; orcid.org/0000-0001-7116-8132

Tobias Borsdorff − *Earth Science Group, SRON Netherlands Institute for Space Research, Leiden 2333, The Netherlands*

Manu Goudar − *Earth Science Group, SRON Netherlands Institute for Space Research, Leiden 2333, The Netherlands*

Christopher F. Lee − *Department of Chemistry, University of Colorado Boulder, Boulder, Colorado 80309-0215, United States; Cooperative Institute for Research in Environmental Sciences, University of Colorado Boulder, Boulder, Colorado 80309-0216, United States*

Theodore K. Koenig − *Department of Chemistry, University of Colorado Boulder, Boulder, Colorado 80309-0215, United States; Cooperative Institute for Research in Environmental Sciences, University of Colorado Boulder, Boulder, Colorado 80309-0216, United States;* Present Address: State Key Joint Laboratory of Environmental Simulation and Pollution Control, BIC-ESAT and IJRC, College of Environmental Sciences and Engineering, Peking University, Beijing 100871, China; orcid.org/0000-0002-3756-4315

Johana Romero-Alvarez − *Department of Chemistry, University of Colorado Boulder, Boulder, Colorado 80309-0215, United States*

Teresa Campos − *Atmospheric Chemistry Observations & Modeling, National Center for Atmospheric Research, Boulder, Colorado 80307, United States*

Christoph Knote − *Faculty of Medicine, University of Augsburg, Augsburg 86159, Germany;* orcid.org/0000-0001-9105-9179

Nicolas Theys − *Royal Belgian Institute for Space Aeronomy (BIRA-IASB), Brussels 1180, Belgium*

Jochen Landgraf − *Earth Science Group, SRON Netherlands Institute for Space Research, Leiden 2333, The Netherlands*

Complete contact information is available at: https://pubs.acs.org/10.1021/acsearthspacechem.2c00048

Author Contributions

R.V. designed the research. N.K., K.J.Z., C.F.L., and R.V. performed field measurements. T.B., M.G., and J.L. processed and distributed TROPOMI CO data. N.T. provided visualization routines and data for the UV−vis TROPOMI instrument. C.K. performed the FLEXPART modeling. T.C. contributed aircraft data. J.P.R. conducted the data analysis, with contributions from K.J.Z. and M.G., and the radiative transfer studies. J.P.R. and R.V. interpreted the data, following discussions with T.B., M.G., J.L., N.T., and K.J.Z. J.P.R., K.J.Z., and R.V. wrote the paper, with contributions from all co-authors.

Notes

The authors declare no competing financial interest.

■ ACKNOWLEDGMENTS

The BB-FLUX project was funded by the National Science Foundation (NSF) grant AGS-1754019. The BB-FLUX dataset is available from https://data.eol.ucar.edu/project/BB-FLUX. This material is based upon work supported by the National Center for Atmospheric Research, which is a major research facility sponsored by the NSF under Cooperative Agreement No. 1852977. Additionally, this research has been funded in part by the TROPOMI national program from the Netherlands Space Office (NSO). N.T. received support from ESA S5P MPC (4000117151/16/I-LG), Belgium Prodex TRACE-S5P (PEA 40001055989). C.F.L. received summer support from the Department of Chemistry at CU Boulder. The TROPOMI preoperational data processing was carried out on the Dutch national E-infrastructure with the support of the SURF Cooperative. The authors also extend their thanks to David Plummer, Larry Oolman, and the entire King Air flight team at the University of Wyoming for their support during the BB-FLUX campaign.

REFERENCES

(1) Andreae, M.; Merlet, P. Emission of trace gases and aerosols from biomass burning. *Global Biogeochem. Cycles* **2001**, *15*, 955−966.

(2) Akagi, S. K.; Yokelson, R. J.; Wiedinmyer, C.; Alvarado, M. J.; Reid, J. S.; Karl, T.; Crounse, J. D.; Wennberg, P. O. Emission Factors for Open and Domestic Biomass Burning for Use in Atmospheric Models. *Atmos. Chem. Phys.* **2011**, *11*, 4039−4072.

(3) Crutzen, P. J.; Andreae, M. O. Biomass Burning in the Tropics: Impact on Atmospheric Chemistry and Biogeochemical Cycles. *Science* **1990**, *250*, 1669−1678.

(4) Chen, J.; Li, C.; Ristovski, Z.; Milic, A.; Gu, Y.; Islam, M.; Wang, S.; Hao, J.; Zhang, H.; He, C.; Guo, H.; Fu, H.; Miljevic, B.; Marawska, L.; Thai, P.; LAM, Y.; Pereira, G.; Ding, A.; Huang, X.; Dumka, U. A review of biomass burning: Emissions and impacts on air quality, health and climate in China. *Sci. Total Environ.* **2017**, *579*, 1000−1034.

(5) Reid, C. E.; Brauer, M.; Johnston, F.; Jerrett, M.; Balmes, J.; Elliott, C. Critical review of health impacts of wildfire smoke exposure. *Environ. Health Perspect.* **2016**, *124*, 1334−1343.

(6) Scholze, M.; Knorr, W.; Arnell, N. W.; Prentice, I. C. A climate-change risk analysis for world ecosystems. *Proc. Natl. Acad. Sci. U.S.A.* **2006**, *103*, 13116−13120.

(7) Li, F.; Zhang, X.; Kondragunta, S. Highly anomalous fire emissions from the 2019-2020 Australian bushfires. *Environ. Res. Commun.* **2021**, *3*, No. 105005.

(8) National Academies of Sciences, Engineering, and Medicine *The Future of Atmospheric Chemistry Research*; The National Academies Press, 2016; p 12.

(9) Borsdorff, T.; Aan De Brugh, J.; Hu, H.; Hasekamp, O.; Sussman, R.; Rettinger, M.; Hase, F.; Gross, J.; Schneider, M.; Garcia, O.; Stremme, W.; Grutter, M.; Feist, D.; Arnold, S.; De Maziére, M.; Sha, M. K.; Pollard, D.; Kiel, M.; Roehl, C.; Wennberg, P.; Toon, G.; Landgraf, J. Mapping carbon monoxide pollution from space down to city scales with daily global coverage. *Atmos. Meas. Tech.* **2018**, *11*, 5507−5518.

(10) Borsdorff, T.; Aan De Brugh, J.; Schneider, A.; Lorente, A.; Birk, M.; Wagner, G.; Kivi, R.; Hase, F.; Feist, D. G.; Sussmann, R.; Rettinger, M.; Wunch, D.; Warneke, T.; Landgraf, J. Improving the TROPOMI CO data product: Update of the spectroscopic database and destriping of single orbits. *Atmos. Meas. Tech.* **2019**, *12*, 5443−5455.

(11) Theys, N.; Volkamer, R.; Müller, J. -F.; Zarzana, K. J.; Kille, N.; Clarisse, L.; De Smedt, I.; Lerot, C.; Finkenzeller, H.; Hendrick, F.; Koenig, T. K.; Lee, C. F.; Knote, C.; Yu, H.; Van Roozendael, M. Global nitrous acid emissions and levels of regional oxidants enhanced by wildfires. *Nat. Geosci.* **2020**, *13*, 681−686.

(12) Guo, X.; Wang, R.; Pan, D.; Zondlo, M. A.; Clarisse, L.; Van Damme, M.; Whitburn, S.; Coheur, P.-F.; Clerbaux, C.; Franco, B.; Golston, L. M.; Wendt, L.; Sun, K.; Tao, L.; Miller, D.; Mikoviny, T.; Müller, M.; Wisthaler, A.; Tevlin, A. G.; Murphy, J. G.; Nowak, J. B.; Roscioli, J. R.; Volkamer, R.; Kille, N.; Neuman, J. A.; Eilerman, S. J.; Crawford, J. H.; Yacovitch, T. I.; Barrick, J. D.; Scarino, A. J. Validation of IASI Satellite Ammonia Observations at the Pixel Scale Using In Situ Vertical Profiles. *J. Geophys. Res.: Atmos.* **2021**, *126*, No. e2020JD033475.

(13) Sha, M. K.; Langerock, B.; Blavier, J.; Blumenstock, T.; Borsdorff, T.; Buschmann, M.; Dehn, A.; De Maziére, M.; Deutscher, N.; Feist, D.; García, O.; Griffith, D.; Grutter, M.; Hannigan, J.; Hase, F.; Heikkienen, P.; Hermans, C.; Iraci, L.; Jeseck, P.; Jones, N.; Kivi, R.; Kumps, N.; Landgraf, J.; Lorente, A.; Mahieu, E.; Makarova, M.; Mellqvist, J.; Metzger, J.; Morino, I.; Nagahama, T.; Notholt, J.; Ohyama, H.; Ortega, I.; Palm, M.; Petri, C.; Pollard, D.; Rettinger, M.; Robinson, J.; Roche, S.; Roehl, C.; Röhling, A.; Rousogeneous, C.; Schneider, M.; Shiomi, K.; SMale, D.; Stremme, W.; Storng, K.; Sussmann, R.; Té, Y.; Uchino, O.; Velazco, V.; Vigouroux, C.; Vrekoussis, M.; Wang, P.; Warneke, T.; Wizenberg, T.; Wunch, D.; Yamanouchi, S.; Yang, Y.; Zhou, M. Validation of methane and carbon monoxide from Sentinel-5 Precursor using TCCON and NDACC-IRWG stations. *Atmos. Meas. Tech.* **2021**, *14*, 6249−6304.

(14) Logan, J. A.; Prather, M. J.; Wofsy, S. C.; McElroy, M. B. Tropospheric Chemistry: A Global Perspective. *J. Geophys. Res.* **1981**, *86*, 7210−7254.

(15) Andreae, M. O. Emission of trace gases and aerosols from biomass burning − An updated assessment. *Atmos. Chem. Phys.* **2019**, *19*, 8523−8546.

(16) Novelli, P. C.; Masarie, K.; Lang, P. Distributions and recent changes of carbon monoxide in the lower troposphere. *J. Geophys. Res.: Atmos.* **1998**, *103*, 19015−19033.

(17) Permar, W.; Wang, Q.; Selimovic, V.; Wielgasz, C.; Yokelson, R.; Hornbrook, R.; Hills, A.; Apel, E.; Ku, I.; Zhou, Y.; Sive, B.; Sullivan, A.; Collet, J.; Campos, T.; Palm, B.; Peng, Q.; Thornton, J.; Garofalo, L.; Farmer, D.; Kreidenweis, S.; Levin, E.; DeMott, P.; Flocke, F.; Fischer, E.; Hu, L. Emissions of Trace Organic Gases From Western U.S. Wildfires Based on WE-CAN Aircraft Measurements. *J. Geophys. Res.: Atmos.* **2021**, *126*, No. e2020JD033838.

(18) Juncosa Calahorrano, J. F.; Lindaas, J.; O'Dell, K.; Palm, B.; Peng, Q.; Flocke, F.; Pollack, I.; Garofalo, L.; Farmer, D.; Pierce, J.; Collett, J.; Weinheimer, A.; Campos, T.; Hornbrook, R.; Hall, S.; Ullmann, K.; Pothier, M.; Apel, E.; Permar, W.; Hu, L.; Hills, A.; Montzka, D.; Tyndall, G.; Thornton, J.; Fischer, E. Daytime Oxidized Reactive Nitrogen Partitioning in Western U.S. Wildfire Smoke Plumes. *J. Geophys. Res.: Atmos.* **2021**, *126*, No. e2020JD033484.

(19) Lindaas, J.; Pollack, I.; Garofolo, L.; Pothier, M.; Farmer, D.; Kreidenweis, S.; Campos, T.; Flocke, F.; Weinheimer, A.; Montzka, D.; Tyndall, G.; Palm, B.; Peng, Q.; Thornton, J.; Permar, W.; Wielgasz, C.; Hu, L.; Ottmar, R.; Restaino, J.; Hudak, A.; Ku, I.; Zhou, Y.; Sive, B.; Sullivan, A.; Collett, J.; Fischer, E. Emissions of Reactive Nitrogen From Western U.S. Wildfires During Summer 2018. *J. Geophys. Res.: Atmos.* **2021**, *126*, No. e2020JD032657.

(20) Volkamer, R.; Kille, N.; Lee, C. F.; Zarzana, K. J.; Koenig, T.; Nutter, R.; Howard, B. J.; Knote, C.; Campos, T. L.; Oolman, L. D.; Plummer, D. M.; Deng, M.; Wang, Z.; Ahmadov, R.; Pierce, B.; Obersteiner, F.; Zahn, A.; Goulden, T.; Hass, B.; Hudak, A.; Restaino, J.; Ottmar, R. D. In *The BB-FLUX Project: How Much Fuel Goes Up in Smoke?*, American Meteorological Society 100th Annual Meeting, 2020.

(21) Volkamer, R.; Romero-Alvarez, L. J.; Kille, N.; Zarzana, K. J.; Rowe, J. P.BB-FLUX Science Team In *Ecosystem on Fire: How Do Smoke Emissions Relate to Heat Produced From Large Wildfires?*, American Meteorological Society 101st Annual Meeting 2021, Online, 9−15 January 2021.

(22) Kille, N.; Zarzana, K. J.; Romero Alvarez, J.; Lee, C. F.; Rowe, J. P.; Howard, B.; Campos, T.; Hills, A.; Hornbrook, R. S.; Ortega, I.; Permar, W.; Ku, I. T.; Lindaas, J.; Pollack, I. B.; Sullivan, A. P.; Zhou, Y.; Fredrickson, C. D.; Palm, B. B.; Peng, Q.; Apel, E. C.; Hu, L.; Collett, J. L., Jr.; Fischer, E. V.; Flocke, F.; Hannigan, J. W.; Thornton, J.; Volkamer, R. The CU Airborne Solar Occultation Flux Instrument: Performance evaluation during BB-FLUX. *ACS Earth Space Chem.* **2022**, *6*, 582−596.

(23) Romero-Alvarez, J.; Kille, N.; Zarzana, K. J.; Lee, C. F.; Rowe, J. P.; Howard, B.; Ahmadov, R.; James, E.; Bela, M.; Knote, C.; Oolman, L.; Plummer, D. M.; Volkamer, R. In *Evaluation of Wildfire Emission Inventories Using Airborne Flux Measurements*, American Meteorological Society Annual Meeting, Online, 11 January 2021.

(24) Zarzana, K. J.; Rowe, J. P.; Lee, C. F.; Koenig, T. K.; Howard, B.; Nutter, R.; Campos, T.; Oolman, L.; Plummer, D. M.; Knote, C.; Theys, N.; Lerot, C.; Van Roozendael, M.; Apel, E. C.; Hombrook, S.; Hills, A. J.; Pollack, I. B.; Lindaas, J.; Fishcher, E. V.; Flocke, F.; Weinheimer, A. J.; Montzka, D. D.; Tyndall, G.; Peng, Q.; Palm, B. B.; Thornton, J. A.; Permer, W.; Hu, L.; Orphal, J.; Volkamer, R. In *Validation of Satellite Measurements in Wildfire Plumes: A First Look Using Aircraft In Situ and Remote Sensing Instruments*, American Meteorological Society Annual Meeting, Online, 11 January 2021.

(25) Veefkind, J. P.; Aben, I.; McMullan, K.; Förster, H.; de Vries, J.; Otter, G.; Claas, J.; Eskes, H. J.; de Haan, J. F.; Kleipool, Q.; van Weele, M.; Hasekamp, O.; Hoogeveen, R.; Landgraf, J.; Snel, R.; Tol, P.; Ingmann, P.; Voors, R.; Kruzinga, B.; Vink, R.; Visser, H.; Levelt, P. F. TROPOMI on the ESA Sentinel-5 Precursor: A GMES mission

https://doi.org/10.1021/acsearthspacechem.2c00048
ACS Earth Space Chem. 2022, 6, 1799−1812

for global observations of the atmospheric composition for climate, air quality and ozone layer applications. *Remote Sens. Environ.* **2012**, *120*, 70−83.
(26) Landgraf, J.; aan de Brugh, J.; Scheepmaker, R.; Borsdorff, T.; Hu, H.; Houweling, S.; Butz, A.; Aben, I.; Hasekamp, O. Carbon monoxide total column retrievals from TROPOMI shortwave infrared measurements. *Atmos. Meas. Tech.* **2016**, *9*, 4955−4975.
(27) Landgraf, J.; aan de Brugh, J.; Borsdorff, T.; Houweling, S.; Hasekamp, O. P. *Algorithm Theoretical Baseline Document for Sentinel-5 Precursor: Carbon Monoxide Total Column Retrieval, ATBD*; SRON: Utrecht, The Netherlands, 2016.
(28) Hu, H.; Hasekamp, O.; Butz, A.; Galli, A.; Landgraf, J.; Aan De Brugh, J.; Borsdorff, T.; Scheepmaker, R.; Aben, I. The operational methane retrieval algorithm for TROPOMI. *Atmos. Meas. Tech.* **2016**, *9*, 5423−5440.
(29) Borsdorff, T.; Aan de Brugh, J.; Hu, H.; Aben, I.; Hasekamp, O.; Landgraf, J. Measuring carbon monoxide with TROPOMI: First results and a comparison with ECMWF-IFS analysis data. *Geophys. Res. Lett.* **2018**, *45*, 2826−2832.
(30) Borsdorff, T.; Andrasec, J.; Aan De Brugh, J.; Hu, H.; Aben, I.; Landgraf, J. Detection of carbon monoxide pollution from cities and wildfires on regional and urban scales: the benefit of CO column retrievals from SCIAMACHY 2.3 μm measurements under cloudy conditions. *Atmos. Meas. Tech.* **2018**, *11*, 2553−2565.
(31) Borsdorff, T.; Reynoso, A. G.; Maldonado, G.; Mar-Morales, B.; Stremme, W.; Grutter, M.; Landgraf, J. Monitoring CO emissions of the metropolis Mexico City using TROPOMI CO observations. *Atmos. Chem. Phys.* **2020**, *20*, 15761−15774.
(32) Wunch, D.; Toon, G.; Blavier, J.; Washenfelder, R. A.; Notholt, J.; Connor, B. J.; Griffith, D. W. T.; Sherlock, V.; Wennberg, P. The total carbon column observing network. *Philos. Trans. R. Soc., A* **2011**, *369*, 2087−2112.
(33) Schneising, O.; Buchwitz, M.; Euter, M.; Bovensmann, H.; Burrows, J. P.; Borsdorff, T.; Deutscher, N. M.; Feist, D. G.; Griffith, D. W. T.; Hase, F.; Hermans, C.; Iraci, L. T.; Kivi, R.; Landgraf, J.; Morino, I.; Notholt, J.; Petri, C.; Pollard, D. F.; Roche, S.; Shiomi, K.; Strong, K.; Sussmann, R.; Velazco, V. A.; Warneke, T.; Wunch, D. A scientific algorithm to simultaneously retireve carbon monoxide and methane from TROPOMI onboard Sentinel-5 Precursor. *Atmos. Meas. Tech.* **2019**, *12*, 6771−6802.
(34) Jin, X.; Zhu, Q.; Cohen, R. C. Direct estimates of biomass burning NOx emissions and lifetimes using daily observations from TROPOMI. *Atmos. Chem. Phys.* **2021**, *21*, 15569−15587.
(35) Griffin, D.; McLinden, C. A.; Dammers, E.; Adams, C.; Stockwell, C. E.; Warneke, C.; Bourgeois, I.; Peischl, J.; Ryerson, T. B.; Zarzana, K. J.; Rowe, J. P.; Volkamer, R.; Knote, C.; Kille, N.; Koenig, T. K.; Lee, C. F.; Rollins, D.; Rickly, P. S.; Chen, J.; Fehr, L.; Bourassa, A.; Degenstein, D.; Hayden, K.; Mihele, C.; Wren, S. N.; Liggio, J.; Akingunola, A.; Makar, P. Biomass burning nitrogen dioxide emissions derived from space with TROPOMI: methodology and validation. *Atmos. Meas. Tech.* **2021**, *14*, 7929−7957.
(36) Van Der Velde, I.; Van Der Werf, G.; Houweling, S.; Eskes, H.; Veefkind, J. P.; Borsdorff, T.; Aben, I. Biomass burning combustion efficiency observed from space using measurements of CO and NO2 by the TROPOspheric Monitoring Instrument (TROPOMI). *Atmos. Chem. Phys.* **2021**, *21*, 597−616.
(37) Vellalassery, A.; Pillai, D.; Marshall, J.; Gerbig, C.; Buchwitz, M.; Schneising, O.; Ravi, A. Using TROPOspheric Monitoring Instrument (TROPOMI) measurements and Weather Research and Forecasting (WRF) CO modelling to understand the contribution of meteorology and emissions to an extreme air pollution event in India. *Atmos. Chem. Phys.* **2021**, *21*, 5393−5414.
(38) Brioude, J.; Arnold, D.; Stohl, A.; Cassiani, M.; Morton, D.; Seibert, P.; Angevine, W.; Evan, S.; Dingwell, A.; Fast, J. D.; Easter, R. C.; Pisso, I.; Burkhart, J.; Wotawa, G. The Lagrangian particle dispersion model FLEXPART-WRF version 3.1. *Geosci. Model Dev.* **2013**, *6*, 1889−1904.
(39) Stohl, A.; Thompson, D. A Density Correction for Lagrangian Particle Dispersion Models. *Boundary-Layer Meteorol.* **1999**, *90*, 155−167.
(40) Stohl, A.; Forster, C.; Frank, A.; Seibert, P.; Wotawa, G. Technical note: The Lagrangian particle dispersion model FLEXPART version 6.2. *Atmos. Chem. Phys.* **2005**, *5*, 2461−2474.
(41) Stohl, A.; Sodemann, H.; Eckhard, S.; Frank, A.; Seibert, P.; Wotawa, G. *The Lagrangian Particle Dispersion Model FLEXPART*, Version 8.2, 2010. http://transport.nilu.no/flexpart.
(42) Westphal, D. L.; Toon, O. Simulations of Microphysical, Radiative, and Dynamical Processes in a Continental-Scale Forest Fire Smoke Plume. *J. Geophys. Res.* **1991**, *96*, No. 22379.
(43) Bela, M. M.; Kille, N.; McKeen, S.; Romero-Alvarez, J.; Ahmadov, R.; James, E.; Pereira, G.; Schmidt, C.; Pierce, R. B.; O'Neill, S. M.; Zhang, X.; Kondragunta, S.; Wiedinmyer, C.; Volkamer, R. Quantifying Carbon Monoxide Emissions on the Scale of Large Wildfires. *Geophys. Res. Lett.* **2022**, *49*, No. e2021GL095831.
(44) Burling, I. R.; Yokelson, R.; Akagi, S.; Urbanski, S.; Wold, C.; Griffith, D.; Johnson, T.; Reardon, J.; Weise, D. Airborne and ground-based measurements of the trace gases and particles emitted by prescribed fires in the United States. *Atmos. Chem. Phys.* **2011**, *11*, 12197−12216.
(45) Hase, F.; Hannigan, J. W.; Coffey, M. T.; Goldman, A.; Höpfner, M.; Jones, N. B.; Rinsland, C. P.; Wood, S. W. Intercomparison of retrieval codes used for the analysis of high-resolution, ground-based FTIR measurements. *J. Quant. Spectrosc. Radiat. Transfer* **2004**, *87*, 25−52.
(46) Rothman, L. S.; Gordon, I. E.; Babikov, Y.; Barbe, A.; Chris Benner, D.; Bernath, P. F.; Birk, M.; Bizzocchi, L.; Boudon, V.; Brown, L. R.; Campargue, A.; Chance, K.; Cohen, E. A.; Coudert, L. H.; Devi, V. M.; Drouin, B. J.; Fayt, A.; Flaud, J. -M.; Gamache, R. R.; Harrison, J. J.; Hartmann, J. -M.; Hill, C.; Hodges, J. T.; Jacquemart, D.; Jolly, A.; Lamouroux, J.; Le Roy, R. J.; Li, G.; Long, D. A.; Lyulin, O. M.; Mackie, C. J.; Massie, S. T.; Mikhailenko, S.; Muller, H. S. P.; Naumenko, O. V.; Nikitin, A. V.; Orphal, J.; Perevalov, V.; Perrin, A.; Polovtseva, E. R.; Richerd, C.; Smith, M. A. H.; Starikova, E.; Sung, K.; Tashkun, S.; Tennyson, J.; Toon, G. C.; Tyuterev, V. l. G.; Wagner, G. The HITRAN2012 molecular spectroscopic database. *J. Quant. Spectrosc. Radiat. Transfer* **2013**, *130*, 4−50.
(47) Veefkind, J. P.; Aben, I.; McMullan, K.; Förster, H.; de Vries, J.; Otter, G.; Claas, J.; Eskes, H. J.; de Haan, J. F.; Kleipool, Q.; van Weele, M.; Hasekamp, O.; Hoogeveen, R.; Landgraf, J.; Snel, R.; Tol, P.; Ingmann, P.; Voors, R.; Kruzinga, B.; Vink, R.; Visser, H.; Levelt, P. F. TROPOMI on the ESA Sentinel-5 Precursor: A GMES mission for global observations of the atmospheric composition for climate, air quality and ozone layer applications. *Remote Sens. Environ.* **2012**, *120*, 70−83.
(48) Wiggins, E. B.; Soja, A. J.; Gargulinski, E.; Halliday, H. S.; Bradley Pierce, R.; Schmidt, C. C.; Nowak, J. B.; Digangi, J. P.; Diskin, G. S.; Katich, J. M.; Perring, A. E.; Schwarz, J. P.; Anderson, B. E.; Chen, G.; Crosbie, E. C.; Jordan, C.; Robinson, C. E.; Sanchez, K. J.; Shingler, T. J.; Shook, M.; Thornhill, K. L.; Winstead, E. L.; Ziemba, L. D.; Moore, R. H. High Temporal Resolution Satellite Observations of Fire Radiative Power Reveal Link Between Fire Behavior and Aerosol and Gas Emissions. *Geophys. Res. Lett.* **2020**, *47*, No. e2020GL090707.
(49) Van Geffen, J.; Boersma, K. F.; Eskes, H.; Sneep, M.; Ter Linden, M.; Zara, M.; Veefkind, P. J. S5P TROPOMI NO2 slant column retrieval: Method, stability, uncertainties and comparisons with OMI. *Atmos. Meas. Tech.* **2020**, *13*, 1315−1335.
(50) De Smedt, I.; Pinardi, G.; Vigouroux, C.; Compernolle, S.; Bais, A.; Benavent, N.; Boersma, F.; Chan, K.-L.; Donner, S.; Eichmann, K.-U.; Hedelt, P.; Hendrick, F.; Irie, H.; Kumar, V.; Lambert, J.-C.; Langerock, B.; Lerot, C.; Liu, C.; Loyola, D.; Piters, A.; Richter, A.; Rivera Cárdenas, C.; Romahn, F.; Ryan, R. G.; Sinha, V.; Theys, N.; Vlietinck, J.; Wagner, T.; Wang, T.; Yu, H.; Van Roozendael, M. Comparative assessment of TROPOMI and OMI formaldehyde observations and validation against MAX-DOAS network column measurements. *Atmos. Chem. Phys.* **2021**, *21*, 12561−12593.

(51) Beirle, S.; Borger, C.; Dörner, S.; Li, A.; Hu, Z.; Liu, F.; Wang, Y.; Wagner, T. Pinpointing nitrogen oxide emissions from space. *Sci. Adv.* **2019**, *5*, No. eaax9800.
(52) ESA (European Space Agency) [dataset]. Copernicus Sentinel-5P: TROPOMI Level 2 Carbon Monoxide Total Column Products. DOI: 10.5270/S5P-1hkp7rp.
(53) SRON: Scientific TROPOMI CO. ftp://ftp.sron.nl/open-access-data-2/TROPOMI/tropomi/co/ (accessed July 15, 2021).
(54) Rothman, L. S.; Gordon, I. E.; Barbe, A.; Chris Benner, D.; Bernath, P. F.; Birk, M.; Boudon, V.; Brown, L. R.; Campargue, A.; Champion, J. -P.; Chance, K.; Coudert, L. H.; Dana, V.; Devi, V. M.; Fally, S.; Flaud, J. -M.; Gamache, R. R.; Goldman, A.; Jacquemart, D.; Kleiner, I.; Lacome, N.; Lafferty, W. J.; Mandin, J. -Y.; Massie, S. T.; Mikhailenko, S. N.; Miller, C. E.; Moazzen-Ahmadi, N.; NAumenko, O. V.; Nitkin, A. V.; Orphal, J.; Perevalov, V. I.; Perrin, A.; Predoi-Cross, A.; Rinsland, C. P.; Rotger, M.; Simeckova, M.; Smith, M. A. H.; Sung, K.; Tashkun, S. A.; Tennyson, J.; Toth, R. A.; Vandaele, A. C.; Vander Auwera, J. The HITRAN 2008 molecular spectroscopic database. *J. Quant. Spectrosc. Radiat. Transfer* **2009**, *110*, 533−572.
(55) Scheepmaker, R. A.; Frankenberg, C.; Galli, A.; Butz, A.; Schrijver, H.; Deutscher, N. M.; Wunch, D.; Warneke, T.; Fally, S.; Aben, I. Improved water vapour spectroscopy in the 4174-4300 cm^{-1} region and its impact on SCIAMACHY HDO/H_2O measurements. *Atmos. Meas. Tech.* **2013**, *6*, 879−894.
(56) Apituley, A.; Pedergnana, M.; Sneep, M.; Veefkind, J. P.; Loyoloa, D.; Landgraf, J.; Borsdorff, T. *Sentinel-5 Precursor/TROPOMI Level 2 Product User Manual Carbon Monoxide*; SRON-S5P-LEV2-MA-002, 2021.
(57) Borsdorff, T.; Hasekamp, O. P.; Wassmann, A.; Landgraf, J. Insights into Tikhonov regularization: application to trace gas column retrieval and the efficient calculation of total column averaging kernels. *Atmos. Meas. Tech.* **2014**, *7*, 523−535.
(58) Krol, M.; Houweling, S.; Bregman, B.; van den Broek, M.; Segers, A.; van Velthoven, P.; Peters, W.; Dentener, F.; Bergamaschi, P. The two-way nested global chemistry-transport zoom model TM5: algorithm and applications. *Atmos. Chem. Phys.* **2005**, *5*, 417−432.
(59) Rodgers, C. D. *Inverse Methods for Atmospheric Sounding, Theory and Practice*; World Scientific Publishing: Singapore-New-Jersey-London-Hong Kong, 2000.
(60) Kaiser, J. W.; Heil, A.; Andreae, M. O.; Benedetti, A.; Chubarova, N.; Jones, L.; Morcrette, J.-J.; Razinger, M.; Schultz, M. G.; Suttie, M.; van der Werf, G. R. Biomass burning emissions estimated with a global fire assimilation system based on observed fire radiative power. *Biogeosciences* **2012**, *9*, 527−554.
(61) Deutschmann, T.; Beirle, S.; Frieß, U.; Grzegorski, M.; Kern, C.; Kritten, L.; Platt, U.; Prados-Román, C.; Pukite, J.; Wagner, T.; Werner, B.; Pfeilsticker, K. The Monte Carlo atmospheric radiative transfer model McArtim: Introduction and validation of Jacobians and 3D features. *J. Quant. Spectrosc. Radiat. Transfer* **2011**, *112*, 1119−1137.

https://doi.org/10.1021/acsearthspacechem.2c00048
ACS Earth Space Chem. 2022, 6, 1799−1812